Progress In Electromagnetics Research M, Vol. 133, 21–31, 2025

(Received 1 January 2025, Accepted 14 March 2025, Scheduled 25 March 2025)

Dual-Circularly Polarized Miniaturized Metasurface-Loaded Rhombic Loop Broadband Antenna for Sub-6 GHz 5G RFEH Applications

Sanjay Kumar Sharma[1], Taimoor Khan[2,*], and Hitendra Singh[1]

[1] *Department of Electronics and Communication Engineering, Maharishi School of Engineering & Technology, Maharishi University of Information Technology, Lucknow, UP, India*
[2] *Department of Electronics and Communication Engineering, National Institute of Technology Silchar, Silchar, Assam, India*

ABSTRACT: In this paper, a dual-circularly polarized (DCP), metasurface-loaded broadband antenna is designed to operate across frequencies covering the Sub-6 GHz 5G band for RF energy harvesting (RFEH) applications. The DCP antenna can collect RF energy both left-hand circularly polarized (LHCP) and right-hand circularly polarized (RHCP) waves by the same antenna. In this view, the antenna structure features two crossed metallic strips enclosed within symmetrically loaded metallic rhombic loops. Unequal strip widths in the rhombic loops enhance gain and improve impedance matching. A partial ground plane on the bottom layer fine-tunes the operating frequency, while the metasurface boosts antenna gain. A prototype with optimized dimensions was fabricated, and the results, both experimental and simulated, demonstrated excellent agreement.

1. INTRODUCTION

Global data traffic is projected to expand more than tenfold in the next five years due to the increasing number of approximately 6 billion cellular users by 2028, the rise of Internet of Things (IoT) applications, and the widespread use of cellular video. Consequently, mobile networks will face significantly higher traffic demands. To address this, fifth-generation (5G) networks are driving advancements in wireless communication with their cutting-edge features, including ultra-high transmission data rates (peak rates of 10 Gbps), exceptionally low latency (1 ms), dense connectivity, enhanced mobility (up to 500 km/h), and extremely low error bit rates [1]. Three distinct bands have been identified in the radio frequency spectrum for 5G communication: Sub-6 GHz lower band (< 1 GHz), Sub-6 GHz mid-band (3.1–6 GHz), and millimeter-wave 5G band (24.25–52.6 GHz). Sub-6 GHz lower band ensures broad coverage, while Sub-6 GHz mid-band extends coverage with acceptable data rates. In contrast, the millimeter-wave 5G band is dedicated to extremely high data-rate transmissions over short distances [2]. The deployment of millions of sensors-equipped IoT devices is gaining popularity in smart cities and other emerging applications nowadays. For powering these sensors, conventional batteries are usually used. Unfortunately, these batteries require frequent charging, and replacement may be impacted too. Thus, it is imperative to design and deploy self-sufficient IoT systems [3]. To accomplish these objectives, one potential method is to adopt a radio-frequency energy harvesting (RFEH) approach. RFEH offers several advantages over other energy harvesting methods, including maximal power conversion efficiency and compatibility with both indoor and outdoor environments. It leverages the growing availability of RF energy produced by sources such as FM radios, TV stations, mobile towers, and Wi-Fi routers, particularly in metropolitan areas. Additionally, RFEH provides environmental independence, making it a versatile and reliable solution. These benefits have increasingly drawn researchers' interest, positioning RFEH as a promising strategy for sustainable energy harvesting [4].

In the RFEH, the radio frequency energy is utilized and converted into electricity in a way that enables small electronic gadgets. Rectenna (antenna-integrated rectifier) is a remarkable tool utilized for RFEH scenarios [5-7]. Antenna and rectifier circuit are crucial components of a rectenna. The antenna captures radio frequency (RF) energy from the surrounding environment, and the rectifier circuit converts this received RF energy into direct current (DC) electricity. The performance of a rectenna can be generally enhanced with an optimized rectifier. Increasing the antenna's gain can improve the power absorption, which is achievable through larger antenna dimensions. However, increasing the size of the antenna limits its practical applications. Circularly polarized antennas are advantageous as they can receive RF energy regardless of the wave's polarization in the environment, enhancing power reception. Consequently, a compact antenna with omnidirectional coverage, circular polarization, and high average gain is ideal for RF energy harvesting applications. Developing an antenna that can harvest sufficient power presents a significant challenge for researchers. This work focuses on the design and analysis of an antenna circuit tailored for efficient energy harvesting [8].

---

* Corresponding author: Taimoor Khan (ktaimoor@gmail.com).

doi:10.2528/PIERM25010104

Published by THE ELECTROMAGNETIC ACADEMY

Recently, there has been significant research interest in metasurface-inspired antennas due to their exceptional features, including low profile, wide bandwidth, excellent radiation gain, and ease of fabrication. These antennas are typically designed using periodic tiny patch unit-cell patterns which exhibit distinct electromagnetic characteristics. They are synthetic sheets with sub-wavelength properties that can influence electromagnetic waves in a manner that natural materials cannot.

The important electromagnetic features of metasurfaces are that they can be constructed with customised permittivity and permeability, allowing for fine control over wave propagation, reflection, and transmission. Metasurfaces can be built to have a certain surface impedance that controls how electromagnetic waves move through the surface, allowing for functions such as perfect absorption, impedance matching, and wavefront shaping. Many metasurfaces have anisotropic reactions, which means that their electromagnetic behaviour changes with direction. These advancements highlight the potential of metasurface designs in addressing diverse requirements for modern communication systems [9]. A metasurface-based triple-polarized antenna is implemented for 5G applications [10]. Here, by merging two innovative metamaterial-based transmission lines (TLs), an integrated metasurface-based structure that includes a three-port feeding network is assembled to achieve both horizontally and vertically polarized radiation. Tran et al. [11] have constructed a metasurface (MS) associated multi-input multi-output (MIMO) antenna for wideband applications under the Sub-6 GHz band. Proper isolation is achieved by grounding the metallic surface of each MIMO element with metallic vias. A compound U-shaped unit cells and square split ring resonator (SSRR) metasurface split beam antenna is designed to obtain multibeam and high gain features [12]. Here, a multi-beam antenna helps to increase the traffic capacity and also avoids interference. A metasurface has also been used to enhance the gain in [13], where a multi-circle sectored metasurface loaded vertical monopole antenna is investigated for improving the gain. A metasurface can also help to achieve the proper isolation between two antennas [14, 15]. In [14], a metasurface is embedded with a multilayer dual-port antenna as a superstrate for the decoupling of two antennas, whereas in [15], insulation gain is improved by a decoupling strip between two antennas and a ground slot. A metasurface antenna with a magneto-dielectric and split-ring resonator (SRR) enhances the gain and impedance bandwidth [16]. However, antennas [11–16] are limited to linear polarization. Also, the antenna in [16] suffers from a complex design with two ports. A linearly polarized antenna cannot receive a circularly polarized wave completely. Hence, the antenna with circular polarization (CP) features helps in collecting maximum energy from the surrounding atmosphere that will help in RFEH applications. A multilayer circularly polarized metasurface antenna with multi-shaped metasurface elements and parasitic elements was proposed for 5G new radio (NR) applications in [17]. Here, the multi-shaped metasurface deposited on the upper layer of the structure enhances various performance characteristics of the antenna. A transparent conformal polarization-conversion metasurface antenna is implemented for 5G applications [18]. Here, three groups of rectangular slots loaded ellipse type of metamaterial unit cells are arranged around the feedline to achieve polarization conversion properties. A leaf shape of metasurface with a hybrid coupler feed network has been implemented with CP characteristics in [19]. An array of leaf-shaped MTS elements create CP characteristics. A hybrid coupler feed helps in enhancing the impedance bandwidth (BW), axial ratio (AR) BW, and gain of the antenna. These antennas [10–19] suffer either from low antenna gain, large antenna dimensions, polarization-sensitive characteristics, or design complexity with multiport excitation or a multilayer approach. Also, a left-hand circularly polarized (LHCP) wave only collects part of the right-hand circularly polarized (RHCP) wave and vice-versa. Hence, the antenna with dual circular polarization includes both left- and right-hand circular polarization characteristics that can harvest the maximum of the received wave of any polarized wave. In this view, designing a dual-circularly polarized broadband antenna with compact dimensions and omnidirectional radiational characteristics is highly essential for RFEH applications.

In this paper, a compact dual circularly polarized broadband antenna is implemented using parasitic-loaded symmetrical rhombic loop antennas with unequal strip widths and a loaded metasurface, designed for Sub-6 GHz 5G energy harvesting (EH) applications. The proposed antenna targets the rapidly evolving mid-range 5G band. The novelty of the design lies in its broadband characteristics combined with dual circular polarization properties, achieved in a compact form factor. Additionally, the antenna's capability to harvest any polarized wave makes it particularly suitable for RF energy harvesting applications. The paper's structure is as follows. Section 2 details the proposed antenna's structural design. Section 3 presents the simulated performance analysis of the antenna. Section 4 discusses experimental validation, including the fabricated prototype and measurement outcomes. Section 5 concludes the paper, followed by references. This work represents a novel contribution by addressing the critical requirements of compactness, polarization versatility, and broadband characteristics essential for 5G and energy harvesting applications.

2. GEOMETRICAL EXPLANATION OF THE ANTENNA

The geometrical description of the proposed antenna is provided in this section. Figure 1 illustrates the schematic view of the antenna. The design is based on a Rogers RO4003 substrate (dielectric constant $\varepsilon_r = 3.55$, loss tangent $\tan\delta = 0.0027$, and thickness of 1.524 mm). Two parasitic-loaded rhombic loop antennas with unequal strip widths are positioned symmetrically on either side of the feedline above the substrate to achieve the desired operating frequency. These unequal strips improve impedance matching, gain, and axial ratio (AR) performance. A fractional ground plane is employed on the underside of the substrate to achieve a wide impedance bandwidth. Additionally, a metasurface composed of rectangular unit cells is placed adjacent to the partial ground plane to enhance the antenna's gain and operating range. To enable dual circular polarization, two metallic cross-strips are positioned at the center of the rhombic loop structures. This arrangement ensures

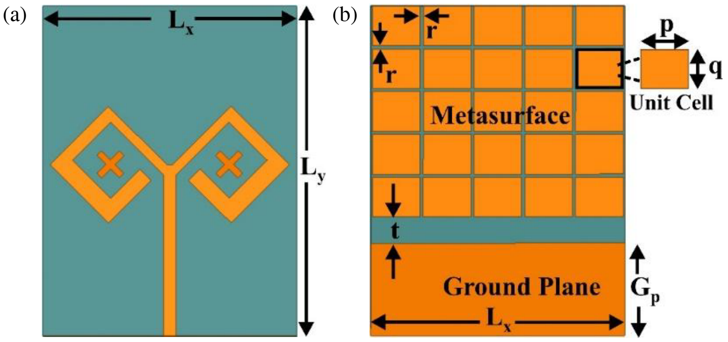

FIGURE 1. Schematic outlook of the projected antenna (a) top-view and (b) bottom-view.

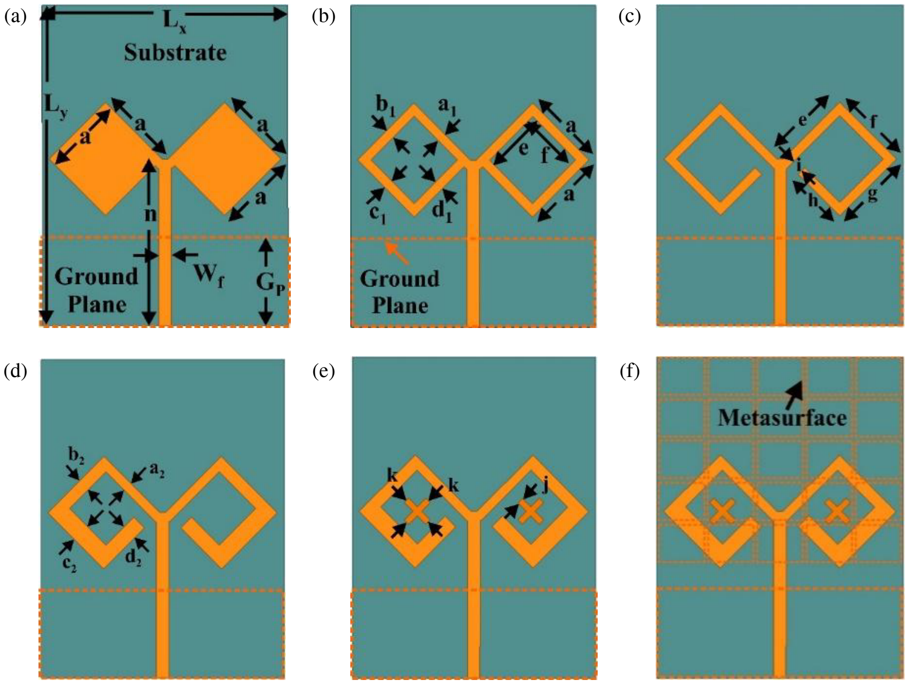

FIGURE 2. Antenna development stages (a) Ant #1, (b) Ant #2, (c) Ant #3, (d) Ant #4, (e) Ant #5, and (f) Ant #6.

optimal performance across the target frequency band. Ansys HFSS simulation tool has been used for designing the antenna. The optimal antenna specifications (all in mm) are as follows: $a_1 = a_2 = 1.5$, $b_1 = 1.5$, $b_2 = 2.5$, $c_1 = 1.5$, $c_2 = 3.5$, $d_1 = 1.5$, $d_2 = 2.5$, $e = 13$, $f = 13$, $g = 13$, $h = 9.5$, $i = 2$, $j = 1$, $k = 5$, $G_p = 14.6$, $W_f = 2$, $n = 27$, $p = 7.5$, $q = 6.25$, $r = 0.5$, $t = 4.15$.

3. SIMULATED PERFORMANCE OF THE ANTENNA

The antenna's development stages are depicted in Figure 2. The corresponding simulated results employed in the staging process are shown in Figure 3. Ant #1 features two rhombic patch structures symmetrically connected to either side of the feedline, along with a partial ground plane. As can be observed, Ant #1 operates at 2.94 GHz frequency with poor impedance bandwidth as well as matching, gain, and AR performances. By creating two symmetrical rhombic loops of slots in both the symmetrical patches of Ant #1 such as in Ant #2, the operating frequency is observed at a higher frequency with increased matching levels, bandwidth, and gain performances comparatively. Ant #3 operates at 3.14 GHz frequency in the operating range of 2.83–3.65 GHz with a maximum gain of 2.70 dBic by introducing a parasitic element onto the two rhombic rings. A large impedance bandwidth within the frequency range of 2.52–3.59 GHz is noted by adjusting the strip widths of the metallic rhombic loop to different values as presented in Ant #4. Also, an increase in gain performance as well as matching levels at the operating frequency is noted. Ant #5 can offer dual-circular polarization (both LHCP and RHCP) characteristics by incorporating two cross-metallic strips within two rhombic loops of structures. Here, a minimum AR value of 0.49 dB is noted within the AR range operating at 3.06–3.78 GHz. Finally, Ant #6 includes a 5×5 rectangular metasurface composed of $7.5 \times 6.25\,\text{mm}^2$ metamaterial unit cells, each positioned ad-

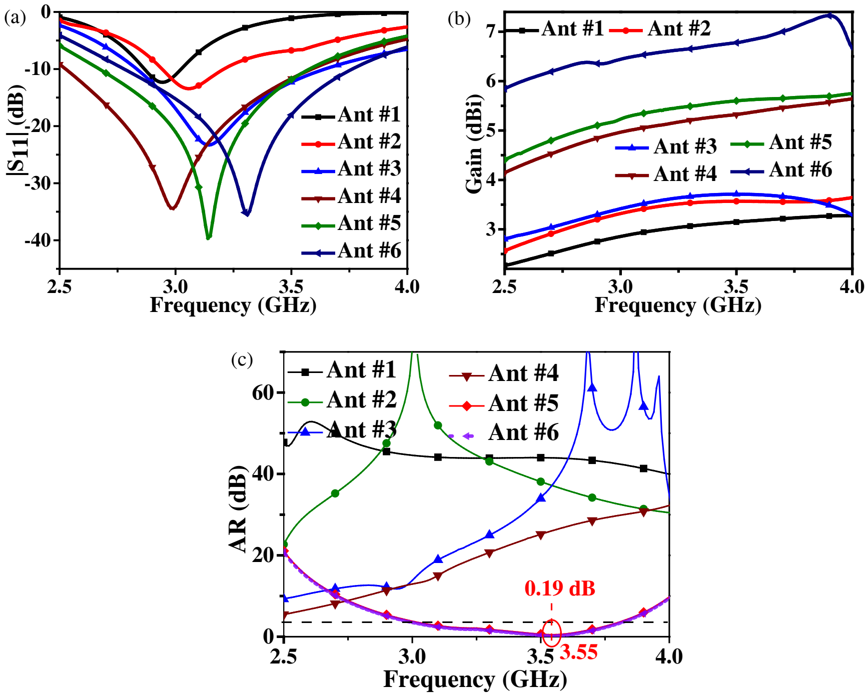

FIGURE 3. Simulated outcomes at various design levels (a) $|S_{11}|$, (b) Gain, and (c) AR.

TABLE 1. Simulated performances in different operating conditions.

Design Steps	Freq. (GHz)	$\lvert S_{11}\rvert$ (dB)	BW (GHz)	Gain (dBic)	AR (dB)	ARBW (GHz)
Ant #1	2.94	−12.31	2.86–3.03	2.9	45.06	-
Ant #2	3.06	−13.43	2.94–3.21	3.37	56.49	-
Ant #3	3.14	−23.28	2.83–3.65	3.55	20.16	-
Ant #4	2.99	−4.41	2.52–3.59	4.95	12.82	-
Ant #5	3.14	−39.64	2.67–3.58	5.38	0.49	3.06–3.78
Ant #6	**3.35**	**−35.54**	**2.77–3.77**	**7.18**	**0.19**	**3.04–3.8**

jacent to the ground plane beneath the substrate. The performance of the antenna in terms of impedance matching and gain was found better with the maximum possible metasurface units. This metasurface significantly enhances the antenna's gain and performance. Metasurface is an artificial periodic architecture that prevents the surface wave created in the substrate by the radiation element and lowers the side lobe level caused by surface wave diffraction at the substrate's edges, resulting in higher antenna gain. It operates within a 2.77–3.77 GHz band with a maximum gain of 7.18 dBic. Also, Ant #6 offers DCP features within the 3.04–3.8 GHz band with the lowest AR value of 0.19 dB. In Table 1, the effectiveness of antennas at various development stages is quantified.

Various parameters that were found important for the antenna design simulation are partial ground plane length (G_p), parasitic element length (i), the gap between metamaterial unit cells (r), Rhombic slots width (w), and width of the feedline (W_f). The implications of altering these different antenna parameters are then examined for variations in aerial simulation performance. The conclusions drawn from this analysis are explained in the subsections that follow:

The 2D radiational patterns of the antennas that are involved in the step-by-step construction stages are plotted in Figure 4. However, the 3D radiational patterns of the antennas that are involved in the step-by-step construction stages are plotted in Figure 5.

3.1. Performance Variation with Ground Plane Length (G_P):

Initially, the optimized antenna is simulated by modifying the partial ground plane length (G_p) value between 12.6 mm and 16.6 mm. The relevant output characteristics are presented in Figure 6. Here, the increase in operating frequency is observed with the increase in G_p value. A suitable impedance matching with a rise in gain is noted with the G_p value of 14.6 mm.

3.2. Performance Variation with Parasitic Element Length (i):

Next, the optimized antenna behavior is characterized by adapting the 'i' value from 1 mm to 3 mm with a step level of 0.5 mm, and the consequences are disclosed in Figure 7. The resonant frequencies are perceived to be at higher frequency levels as the length 'i' is increasing within the range of values. However, the

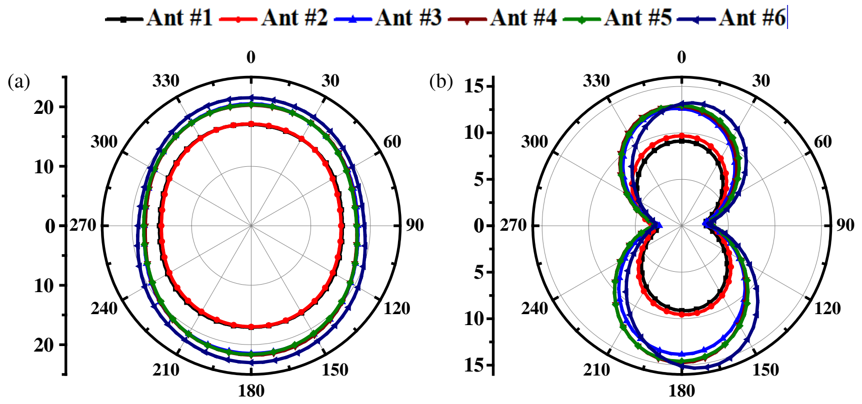

FIGURE 4. 2D radiational patterns of the realized gain at various design levels of step-by-step mechanism (a) H-plane and (b) E-plane.

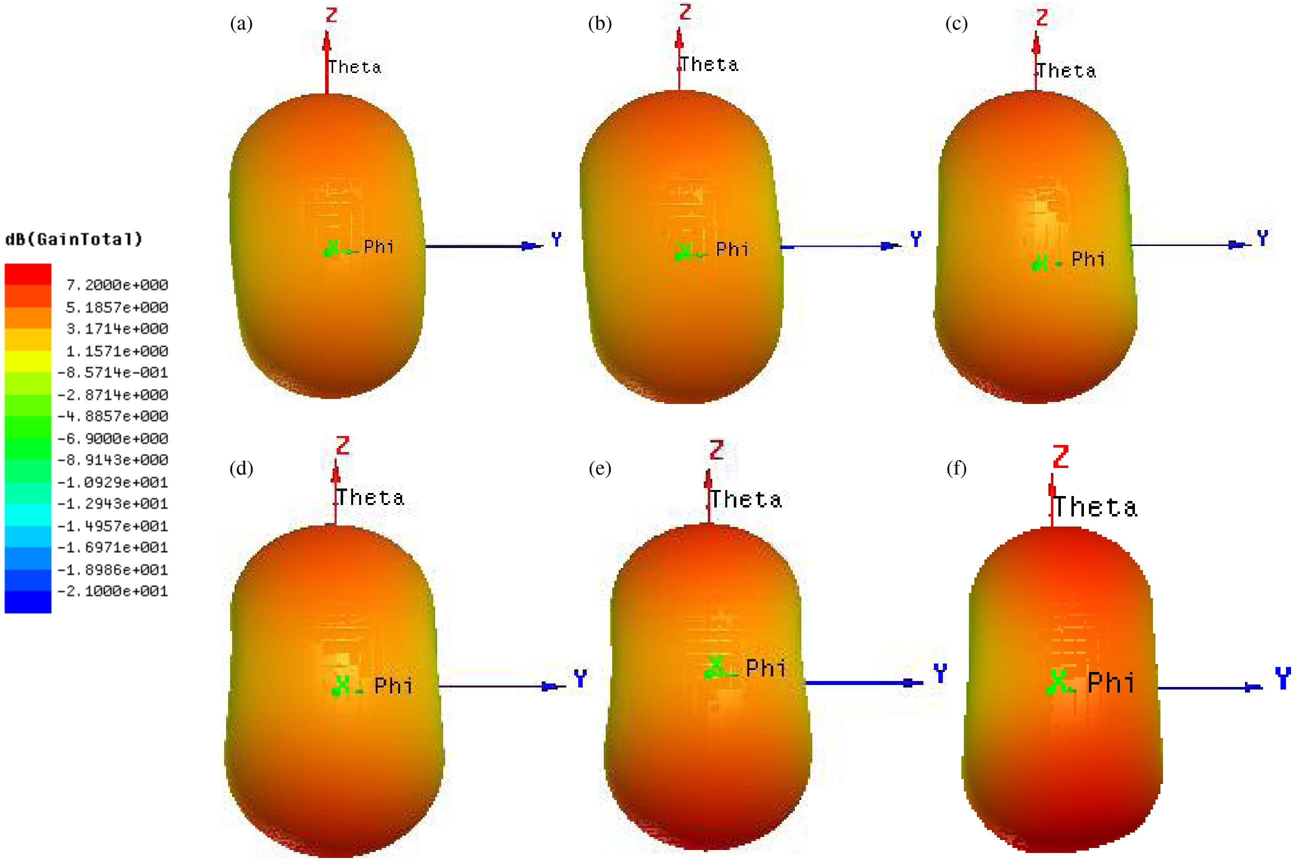

FIGURE 5. 3D radiational patterns of the realized gain at various design levels of step-by-step mechanism (a) Ant #1, (b) Ant #2, (c) Ant #3, (d) Ant #4, (e) Ant #5, and (f) Ant #6.

matching levels are increasing as the 'i' value intensifies from 1 mm to 2.5 mm. Beyond that, the matching value is reduced significantly. Satisfactory outcomes are notified with a gap of 2 mm, and consequently, it is considered an augmented measurement.

3.3. Performance Variation with Gap between Metamaterial Unit Cells (r):

Next, the performance of the antenna is studied by varying the gap 'r' between the metamaterial unit cells from 0.3 mm to 0.7 mm. The $|S_{11}|$ and gain performance outcomes for various 'r' values are shown in Figure 8. It is noted that the operating frequency and matching performance increase with the rise in the 'r' value from 0.3 mm to 0.6 mm. Beyond it, matching performance is degraded by a small value. The greatest value of gain is observed with a gap 'r' value of 0.5 mm.

3.4. Performance Variation with Rhombic Slots Width (w)

Next, the effect of the rhombic slot width on the antenna performance is characterized by changing its range from 8 mm

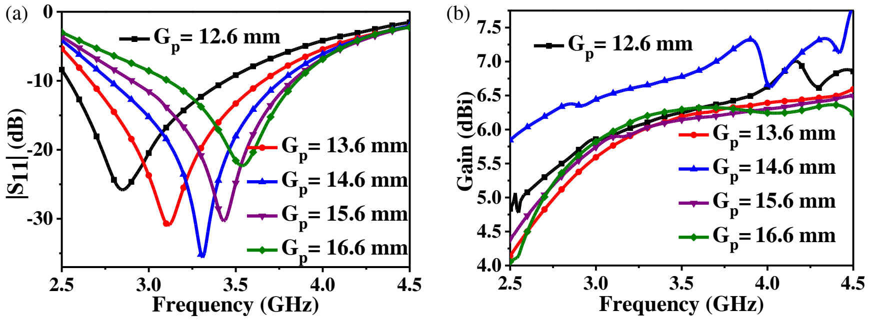

FIGURE 6. Impact of ground plane length. (a) $|S_{11}|$ and (b) Gain.

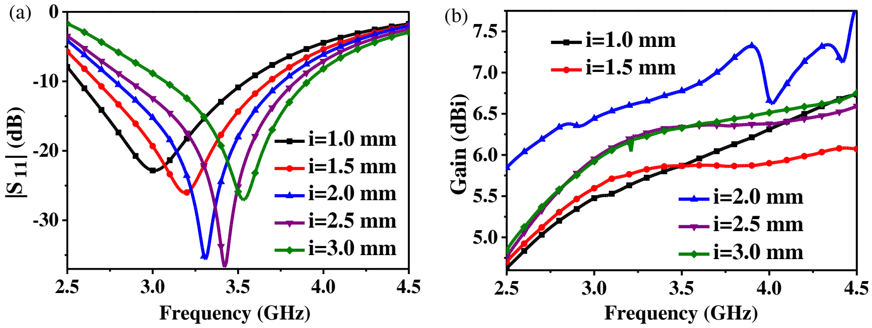

FIGURE 7. Impact of parasitic element length. (a) $|S_{11}|$, (b) Gain.

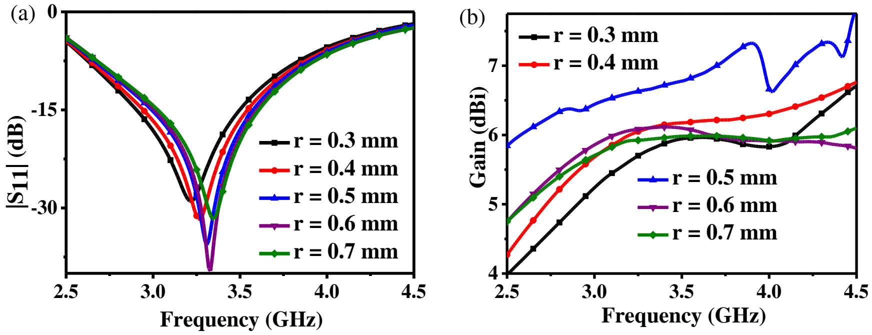

FIGURE 8. Result of ground plane length. (a) $|S_{11}|$, (b) Gain.

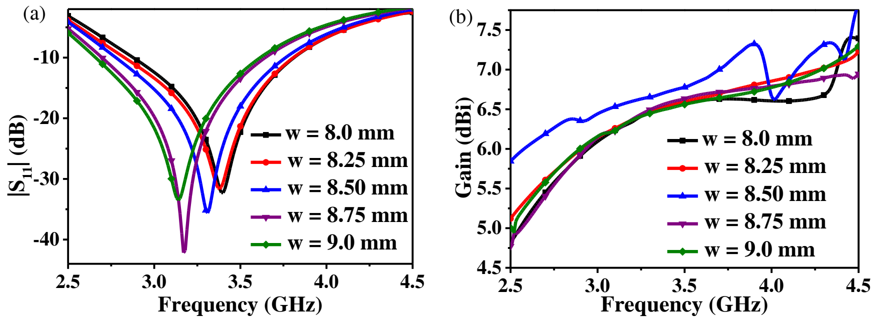

FIGURE 9. Result of Rhombic slot width. (a) $|S_{11}|$, (b) Gain.

to 9 mm, and the relevant performance characteristics are presented in Figure 9. Here it is observed that even though a negligible variation in impedance bandwidth in performance is noted, the resonance is observed at lower operating frequencies as the width increases. A considerable variation in gain value is observed for a width value of 8.5 mm, and hence it is considered as the optimized dimension of the antenna.

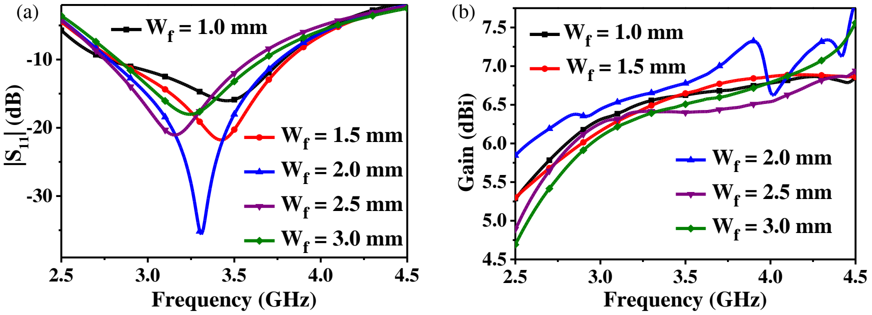

FIGURE 10. Result of feedline width. (a) $|S_{11}|$, (b) Gain.

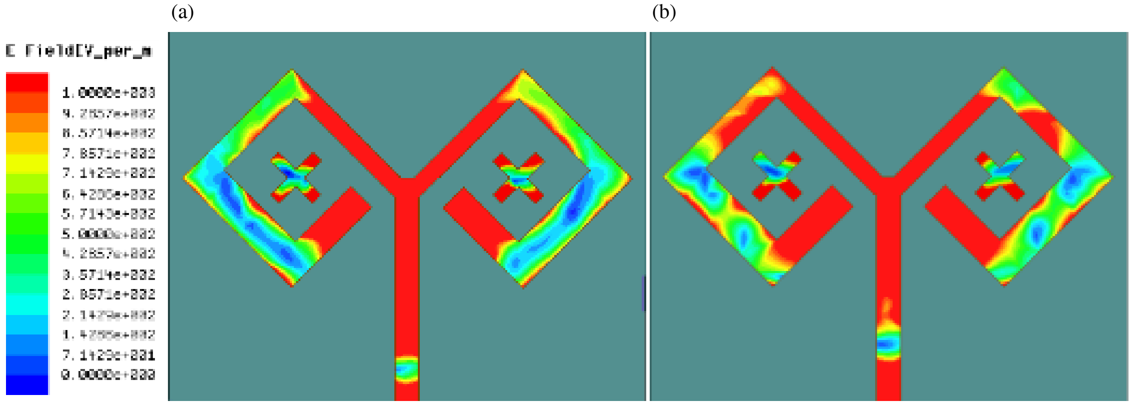

FIGURE 11. E-field strength at 3.5 GHz frequency. (a) Without metamaterial unit cells. (b) With metamaterial unit cells.

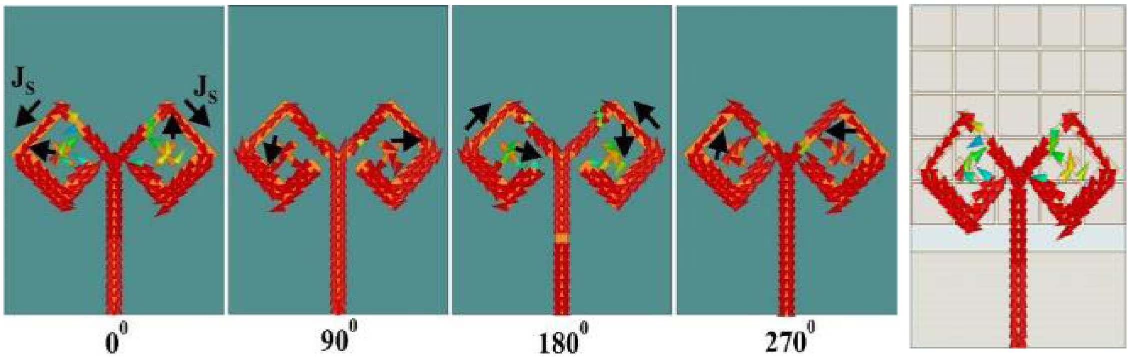

FIGURE 12. E-field distribution patterns of the intended antenna at 3.5 GHz.

3.5. Performance Variation with Feedline Width (W_f)

Finally, the influence of feedline width on antenna performance is investigated by varying it from 1 mm to 3 mm. Figure 10 depicts the key performance factors. As the W_f value increases from 1 mm to 2 mm, the resonant frequencies are observed at lower values with increased impedance matching levels. Beyond 2 mm, matching levels decrease with increased width values. High gain performance values are noted with the feedline width value of 2 mm.

To understand the effect of incorporating metamaterial unit cells, an electric field representation of the proposed antenna without and with metamaterial unit cells has been represented in Figure 11, where the effect of merging metamaterial unit cells is visible with increasing E-field strength onto the antenna radiator. Resultantly, a small enhancement in gain is noted.

The surface current circulation of the presented antenna is noticed at different phase angles (θ) of the antenna, as illustrated in Figure 12. It is observed that as the phase angle changes from 0 to 360 degrees, the orientation of the J_S in the left half of the antenna rotates in a counterclockwise direction, and the orientation of J_S in the right half of the antenna rotates in the clockwise direction. This shows that the left portion of the presented antenna exhibits right-hand circular polarization (RHCP), and the right portion of the antenna offers left-hand circular polarization (LHCP) characteristics. Hence, the resultant antenna offers dual circular polarization (DCP) characteristics, and this characteristic helps to receive any polarized EM

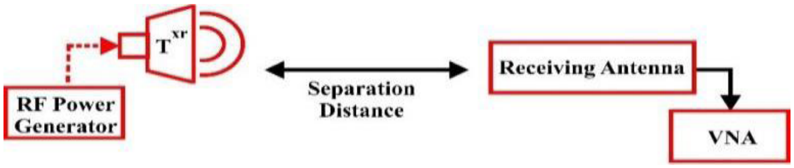

FIGURE 13. Experimental setup for the antenna system.

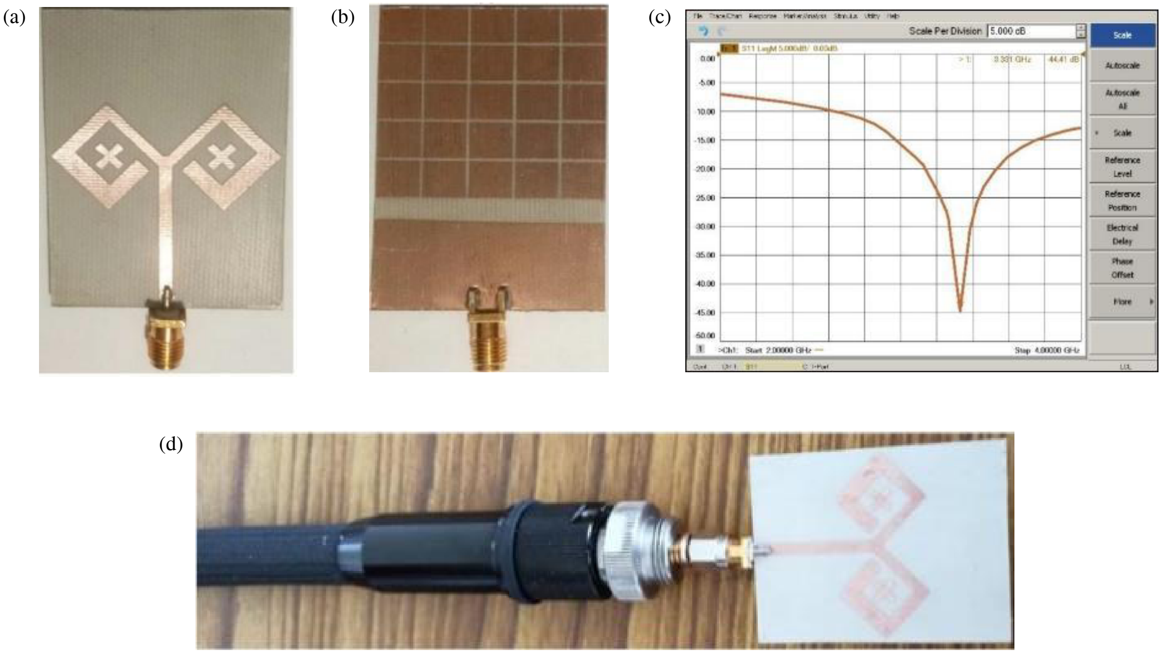

FIGURE 14. Invented antenna. (a) Top view. (b) Bottom view. (c) Measured $|S_{11}|$ value, and (d) $|S_{11}|$ measurement using VNA.

wave. This is an interesting phenomenon of the designed antenna.

4. EXPERIMENTAL VALIDATION OF THE ANTENNA

An experimental measurement setup of the antenna is presented in Figure 13. A tentative measurement setup has been formed to measure the gain value within an anechoic chamber, as revealed in Figures 14(a) and (b). A horn antenna is employed for transmitting purposes, and the developed antenna is used for receiving purposes. The receiving antenna is placed 1.5 meters away from the transmitter, and the gain of the receiving antenna is measured experimentally using the FRIIS free space equation as 7.42 dBic. The axial ratio performance of the antenna has also been measured experimentally within the operating range, and the corresponding obtained AR bandwidth lies within the 3.05–3.78 GHz band. The measured return loss performance outcome is presented in Figure 14(c), and the return loss of the fabricated mast is practically verified using VNA, as shown in Figure 14(d).

The gain measurement setup is created in an anechoic chamber, as revealed in Figure 15. The performance of the fabricated antenna is compared with its simulated performance outcomes, as described in Figure 16. From the experimental measurement outcomes, it should be noted that the fabricated antenna operates over a wide operating range lying between 2.64–4.10 GHz with the least observed $|S_{11}|$ value of -45 dB at the resonance frequency of 3.37 GHz. From the analysis, it can be observed that simulated AR bandwidth is 3.04–3.8 GHz, and measured one is 3.05–3.78 GHz.

Additionally, the simulation antenna's 2D radiational performance is examined; the results are shown in Figure 17. It illustrates how the radiation in the E- and H-planes resembles omnidirectional radiation in its characteristics. As a result, the radiation is visible from all sides. It may receive RF energy from any of its directions, and hence the proposed aerial is appropriate for absorbing RF energy from all directions irrespective of the type of source used for radiation. Hence, it is suitable for RFEH applications. Similarly, co- and cross-polarization characteristics of the antenna are presented in Figure 18. Co-polarization refers to the antenna's E or H fields in the intended direction, i.e., the antenna's emission in the direction of preference. Cross-polarization, on the other hand, refers to the antenna E or H fields in the orthogonal direction, i.e., the antenna's radiation in undesirable directions, and is primarily regarded as an absorption in antenna radiation.

There has been a comparison of the novelty of the proposed metasurface antenna with the existing works. The performance comparison findings are numerically reported in Table 2. The Table indicates that, in comparison to the proposed work, the reported antennas either have a weak gain [11, 15, 16]

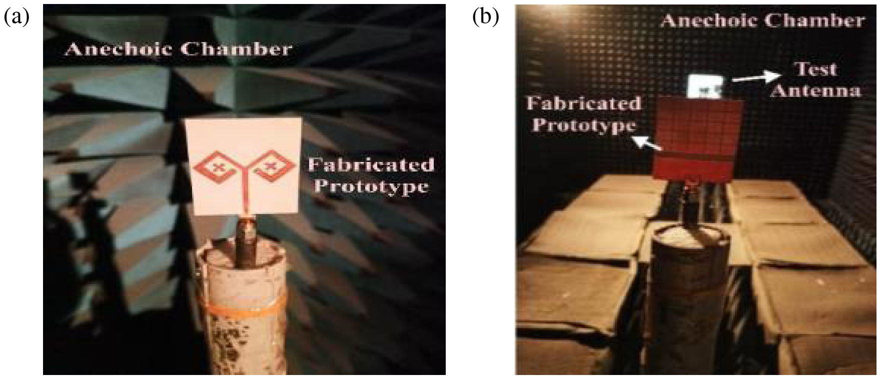

FIGURE 15. Gain measurement setup in the Anechoic Chamber. (a) Front-view. (b) Back-view.

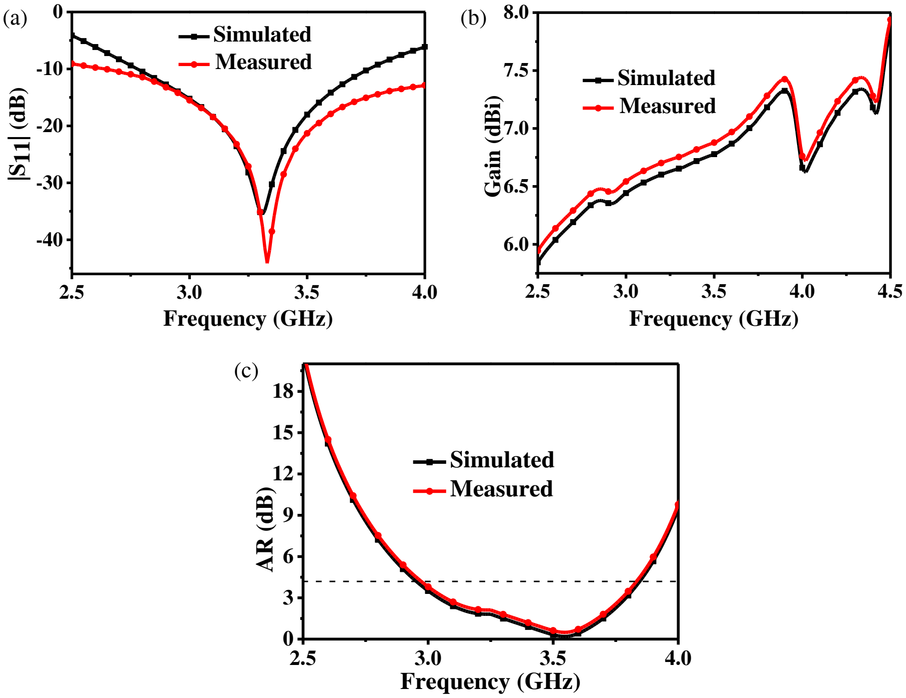

FIGURE 16. Performance comparison analysis. (a) $|S_{11}|$. (b) Gain, and (c) AR.

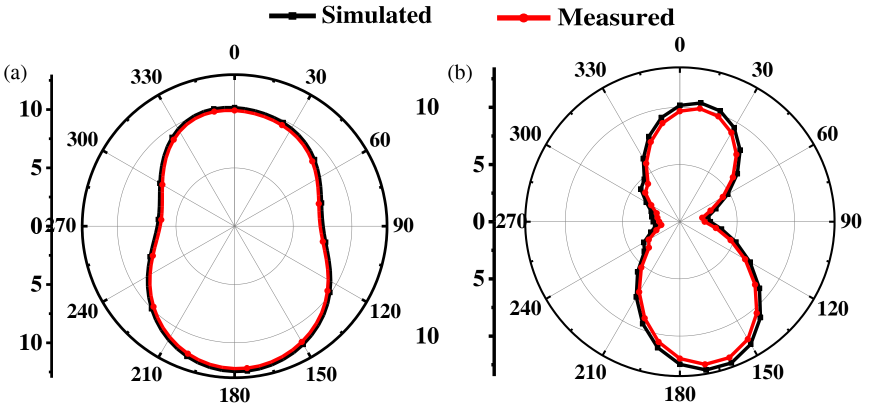

FIGURE 17. Augmented antenna radiation characteristics at 3.5 GHz. (a) $\phi = 0^\circ$ and (b) $\phi = 90^\circ$.

TABLE 2. Performance estimation with presented works.

Ref.	Freq. (GHz)	FBW (%)	Dimension (in terms of λ_0^3)	Gain (dBi)	AR (dB)	ARBW (GHz)
[10]	3.5	16.85	$0.93\lambda_0 \times 0.93\lambda_0 \times 0.056\lambda_0$	10.3	–	–
[11]	3.85	17.14	$0.74\lambda_0 \times 0.42\lambda_0 \times 0.028\lambda_0$	4.1	–	–
[12]	3.5	1.63	$0.62\lambda_0 \times 0.48\lambda_0 \times 0.22\lambda_0$	6.74	–	–
[14]	3.5	11.43	$2.33\lambda_0 \times 1.16\lambda_0 \times 0.36\lambda_0$	7.2	–	–
[15]	3.5	6.80	$0.82\lambda_0 \times 0.45\lambda_0 \times 0.037\lambda_0$	4.88	–	–
[16]	3.5	10.28	$0.353\lambda_0 \times 0.353\lambda_0 \times 0.05\lambda_0$	4.33	–	–
[17]	3.7	40.54	$1.16\lambda_0 \times 1.16\lambda_0 \times 0.056\lambda_0$	7.2	0.5	35.94
[18]	–	24.28	$0.036\lambda_0 \times (0.46\lambda_0)^2 \times 0.036\lambda_0$	5.5	1.2	22.85
[19]	3.9	62.50	$1.4\lambda_0 \times 1.4\lambda_0 \times 0.0467\lambda_0$	9.04	1.2	18.97
Proposed	3.5	44.24	$0.46\lambda_0 \times 0.56\lambda_0 \times 0.018\lambda_0$	7.18	0.25	22.72

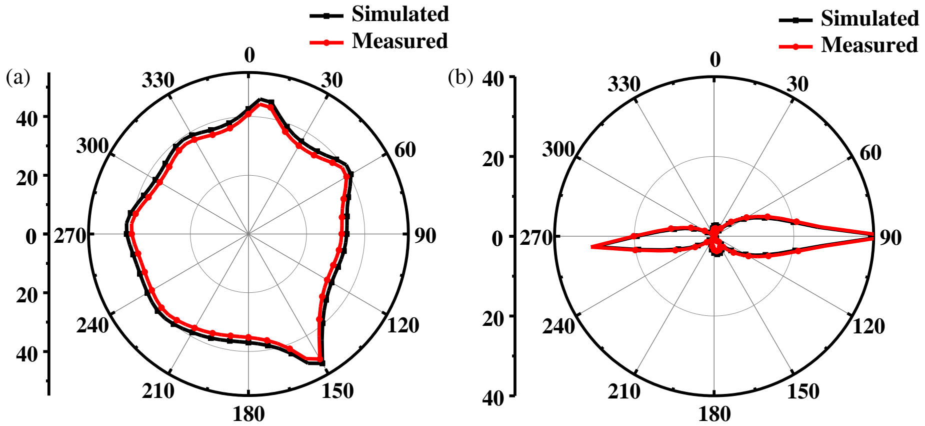

FIGURE 18. Augmented antenna characteristics at 3.5 GHz. (a) Co-polarization and (b) Cross-polarization.

or polarization sensitivity [10–16] issues. A few of the reported antennas were developed using multiport feeding mechanisms [10, 11, 14, 19], multilayer approach [12–14, 17, 19], and coaxial probe feeding [18], hence developing a prototype antenna of these antennas is complex. Also, all the reported antennas mentioned in Table 2 suffer from large antenna dimensions. The presented antenna in this work overcomes all the difficulties and issues, and hence it is found suitable for RFEH applications.

5. CONCLUSION

In this work, a compact dual circularly polarized antenna has been implemented for Sub-6 GHz 5G RFEH applications for the first time. A dual-rhombic loop structure with a loaded metasurface is used for the antenna design. Two cross strips are enclosed within two symmetrical rhombic loop structures to achieve DCP characteristics. A metasurface structure is employed to enhance the antenna's gain. A unique feature of the proposed antenna is its ability to receive both left- and right-hand circularly polarized waves in all directions, as observed from its radiation characteristics. The prototype has been developed with optimized dimensions and validated by comparing the measured and simulated performance outcomes. A good agreement is noted between their performance characteristics.

REFERENCES

[1] Cisco Systems. Mobile Visual Networking Index (VNI) Forecast Project 7-Fold Increase in Global Mobile Data Traffic from 2016–2021, Available at https://newsroom.cisco.com/press-release-content?articleId=1819296.

[2] Surender, D., M. A. Halimi, T. Khan, F. A. Talukdar, Nasimuddin, and S. R. Rengarajan, "5G/Millimeter-wave rectenna systems for radio-frequency energy harvesting/wireless power transmission applications: An overview," *IEEE Antennas and Propagation Magazine*, Vol. 65, No. 3, 57–76, Jun. 2023.

[3] Surender, D., M. A. Halimi, T. Khan, F. A. Talukdar, S. K. Koul, and Y. M. M. Antar, "2.45 GHz Wi-Fi band operated circularly polarized rectenna for RF energy harvesting in smart city applications," *Journal of Electromagnetic Waves and Applications*, Vol. 36, No. 3, 407–423, 2022.

[4] Surender, D., M. A. Halimi, T. Khan, F. A. Talukdar, and Y. M. M. Antar, "A 90° twisted quarter-sectored compact and circularly polarized DR-rectenna for RF energy harvesting applications," *IEEE Antennas and Wireless Propagation Letters*, Vol. 21, No. 6, 1139–1143, 2022.

[5] Surender, D., M. A. Halimi, T. Khan, F. A. Talukdar, B. K. Kanaujia, K. Rambabu, and A. A. Kishk, "Analysis of facet-loaded rectangular DR-rectenna designs for multisource RF energy-harvesting applications," *IEEE Transactions on Antennas and Propagation*, Vol. 71, No. 2, 1273–1284, Feb. 2023.

[6] Surender, D., M. A. Halimi, T. Khan, F. A. Talukdar, and Y. M. M. Antar, "Circularly polarized DR-rectenna for 5G and

Wi-Fi bands RF energy harvesting in smart city applications," *IETE Technical Review*, Vol. 39, No. 4, 880–893, 2022.

[7] Surender, D., T. Khan, F. A. Talukdar, A. De, Y. M. M. Antar, and A. P. Freundorfer, "Key components of rectenna system: A comprehensive survey," *IETE Journal of Research*, Vol. 68, No. 5, 3379–3405, 2022.

[8] Surender, D., T. Khan, F. A. Talukdar, and Y. M. M. Antar, "Rectenna design and development strategies for wireless applications: A review," *IEEE Antennas and Propagation Magazine*, Vol. 64, No. 5, 16–29, Oct. 2022.

[9] Liu, W. E. I., Z. N. Chen, X. Qing, J. Shi, and F. H. Lin, "Miniaturized wideband metasurface antennas," *IEEE Transactions on Antennas and Propagation*, Vol. 65, No. 12, 7345–7349, Dec. 2017.

[10] Wang, Z., S. Liu, and Y. Dong, "Low-profile metasurface-based antenna with tripolarization for 5G applications," *IEEE Transactions on Antennas and Propagation*, Vol. 69, No. 9, 5437–5445, Sep. 2021.

[11] Tran, H.-H., T. T.-L. Nguyen, H.-N. Ta, and D.-P. Pham, "A metasurface-based MIMO antenna with compact, wideband, and high isolation characteristics for sub-6 GHz 5G applications," *IEEE Access*, Vol. 11, 67 737–67 744, 2023.

[12] Fadhil, T. Z., N. A. Murad, M. K. A. Rahim, M. R. Hamid, and L. O. Nur, "A beam-split metasurface antenna for 5G applications," *IEEE Access*, Vol. 10, 1162–1174, 2021.

[13] Luo, Y., Y. Wang, N. Yan, W. An, and K. Ma, "A broadband gain-enhanced conical-beam antenna loaded with the multicircle sectored metasurface," *IEEE Transactions on Antennas and Propagation*, Vol. 71, No. 7, 5542–5548, Jul. 2023.

[14] Guo, J., F. Liu, L. Zhao, Y. Yin, G.-L. Huang, and Y. Li, "Metasurface antenna array decoupling designs for two linear polarized antennas coupled in H-plane and E-plane," *IEEE Access*, Vol. 7, 100 442–100 452, 2019.

[15] Hu, Y., W. H. Chen, M. Q. Wu, L. H. Ye, F. Jiang, J.-F. Li, and D.-L. Wu, "Isolation enhancement between two low-profile patch antennas for in-band full-duplex applications," *IEEE Antennas and Wireless Propagation Letters*, Vol. 23, No. 6, 1919–1923, 2024.

[16] Adhiyoga, Y. G., S. F. Rahman, C. Apriono, and E. T. Rahardjo, "Miniaturized 5G antenna with enhanced gain by using stacked structure of split-ring resonator array and magneto-dielectric composite material," *IEEE Access*, Vol. 10, 35 876–35 887, 2022.

[17] Supreeyatitikul, N., T. Lertwiriyaprapa, N. Chudpooti, M. Krairiksh, and C. Phongcharoenpanich, "Broadband multi-shaped metasurface circularly polarized antenna with suppressed non-CP radiation modes," *IEEE Open Journal of Antennas and Propagation*, Vol. 4, 900–911, 2023.

[18] Liu, T., L. Liu, H. Chen, H. Sun, Z. Jin, L. F. Chernogor, D. O. Batrakov, and Z. Sun, "A broadband circularly polarized antenna based on transparent conformal metasurface," *IEEE Antennas and Wireless Propagation Letters*, Vol. 22, No. 12, 3197–3201, Dec. 2023.

[19] Supreeyatitikul, N., P. Janpangngern, T. Lertwiriyaprapa, M. Krairiksh, and C. Phongcharoenpanich, "CMA-based quadruple-cluster leaf-shaped metasurface-based wideband circularly-polarized stacked-patch antenna array for sub-6 GHz 5G applications," *IEEE Access*, Vol. 11, 14 511–14 523, 2023.